**Wind and Structures**, *Vol. 20, No. 1 (2015) 37-58*
DOI: http://dx.doi.org/10.12989/was.2015.20.1.037


# Detached eddy simulation of flow around rectangular bodies with different aspect ratios

Hee Chang Lim*[1] and Masaaki Ohba[2a]

[1]*School of Mechanical Engineering, Pusan National University, San 30, Jangjeon-Dong, Geumjeong-Gu, Busan, 609-735, South Korea*
[2]*Department of Architecture, Faculty of Engineering, Tokyo Polytechnic University, Atsugi, Kanagawa, 243-02/3, Japan*

*(Received March 14, 2014, Revised September 10, 2014, Accepted November 1, 2014)*

**Abstract.** As wind flows around a sharp-edged body, the resulting separated flow becomes complicated, with multiple separations and reattachments as well as vortex recirculation. This widespread and unpredictable phenomenon has long been studied academically as well as in engineering applications. In this study, the flow characteristics around rectangular prisms with five different aspect ratios were determined through wind tunnel experiments and a detached eddy simulation, that placed the objects in a simulated deep turbulent boundary layer at $Re = 4.6 \times 10^4$. A series of rectangular prisms with the same height ($h$ = 80 mm), different longitudinal lengths ($l$ = 0.5$h$, $h$, and 2$h$), or different transverse widths ($w$ = 0.5$h$, $h$, and 2$h$) were employed to observe the effects of the aspect ratio. Furthermore, five wind directions (0°, 10°, 20°, 30°, and 45°) were selected to observe the effects of the wind direction. The simulated results of the surface pressure were compared to the wind tunnel experiment results and the existing results of previous papers. The vortex and spectrum were also analyzed to determine the detailed flow structure around the body. The paper also highlights the pressure distribution around the rectangular prisms with respect to the different aspect ratios. With an increasing transverse width, the surface suction pressure on the top and side surfaces becomes stronger. In addition, depending on the wind direction, the pressure coefficient experiences a large variation and can even change from a negative to a positive value on the side surface of the cube model.

**Keywords:** rectangular prisms; flow characteristics; aspect ratio; wind direction; wind-tunnel test; detached-eddy simulation

## 1. Introduction

With regard to the turbulent boundary layer flow around a bluff body, we know that the flow separates at the front surface of the body and then reattaches after passing the body or floats and entrains downstream. In addition, multiple vortex recirculation regions are formed around the bluff body, as shown in Yakhot *et al*. (2006a). This type of complicated flow phenomena plays an important role in the design and development of practical objects such as buildings, vehicles, and bridges. Therefore, an increasing amount of academic scholars and application engineers are focusing on this topic. However, more academic effort is still needed to make further progress. In

*Corresponding author, Associate Professor, E-mail: hclim@pusan.ac.kr
[a] Professor, E-mail: ohba@arch.t-kougei.ac.jp

**Copyright © 2015 Techno-Press, Ltd.**
http://www.techno-press.org/?journal=was&subpage=8 ISSN: 1226-6116 (Print), 1598-6225 (Online)

earlier studies, Castro and Robins (1977) (hereafter denoted by CR) investigated the flow characteristics around surface-mounted cubes in both uniform and deep turbulent boundary layers by performing wind tunnel experiments, which demonstrated the importance of an appropriate atmospheric boundary layer and addressed the effects of the Reynolds number. Later researchers often compared their results with Castro and Robins' results on the surface pressure distribution and the mean and fluctuating velocities within the wake. For example, Lim *et al*. (2007) (hereafter, LCH) investigated the extant Reynolds number issues in detail. Furthermore, Lim (2009) continued to investigate the surface pressure distribution, changing the shape of the bodies under similar inlet boundary conditions as in CR.

There have been many studies conducted to investigate the complex turbulent flow characteristics around surface-mounted bluff bodies. Schofield and Logan (1990) analysed the turbulent shear flow over surface-mounted obstacles. Their study concentrated on how major features of the flow are influenced by the model geometry and the conditions of the incident turbulent flow. Some papers have observed the interaction of the turbulent flow and rectangular bodies. Tieleman and Akins (1996) reported that the variation of the base/side surface pressure of surface-mounted rectangular prisms was determined by the interaction of the incident turbulence with the separated shear layers (that is, the small-scale turbulence, which could be quantified by the modified parameter, $S$). This is particularly true for those flows in which the shear layers arising from the separation of the boundary layers at the salient edges of the body roll up rapidly to form concentrated, relatively steady vortical regions. Martinuzzi and Tropea (1993) investigated the flow around the surface-mounted prismatic obstacles with different span-wise dimensions to observe the effects of the aspect ratios ($w/h$). According to the pressure measurements and vortex visualization results, the aspect ratios have a significant influence on the flow characteristics in terms of the separation, the pressure recovery and the wake region. Further studies have also been conducted by Hussein and Martinuzzi (1996). They presented the energy balance (e.g., the turbulence kinetic energy and the turbulence dissipation rate) around a cube in the turbulent boundary layer, which provided additional explanation of the major flow features. More recently, Cigada *et al*. (2006) investigated the fluid-dynamic forces acting on a rectangular cylinder for unbounded flow conditions. In particular, they focused on the effects of a fixed wall placed at various distances from a rectangular cylinder and observed that the frequency that depends on the force components acting on the cylinder provides the dynamic characterization of the loading and of the wake shedding. In addition, the aspect ratio of the body governs the effects of the wall condition on the force coefficients and the Strouhal Number. Larose and Auteuil (2008) made wind-tunnel measurements on rectangular prisms with aspect ratios of 2, 3 and 4 at high Reynolds numbers, and reported that the Reynolds number effects in terms of $C_L$ and $C_D$ were interestingly not observed in the range of $0.4 \times 10^6$ to $1.0 \times 10^6$. Matsumoto *et al*. (2008) observed the vortex-induced excitation and Karman vortex excitation around the 2D rectangular cylinder with the aspect ratio of 4 and investigated the role of vortex generation on the torsional flutter instability by changing the rotation axis; their work showed that the vortex-induced excitation triggered the torsional flutter instability. In addition, Richards *et al*. (2007) observed the flow characteristics around the bluff prisms with a variety of wind directions, which demonstrated some differences between the mean and peak pressure distributions. Furthermore, their work confirmed the effects of the incident turbulent boundary conditions.

With the rapid development of computational technology, numerical simulations are becoming increasingly popular. However, choosing a turbulence model that can provide an accurate numerical calculation has become a difficult problem. Previously, the predictions of both a

Reynolds-averaged Navier–Stokes (RANS) model and a large-eddy simulation (LES) were popularly used (e.g., see Rodi 1997) to calculate such types of turbulent flow around a surface-mounted bluff body. Compared to the LES model results, the RANS model demonstrated some unreliable results, as shown in Tominaga and Stathopoulos (2010). Due to the limitations of the RANS model and the large amount of time and computational space required for an LES calculation, a hybrid LES/RANS turbulence model was developed and verified to be a promising tool for simulating such types of complicated flows; this hybrid method is known as the detached eddy simulation (DES), as shown in Spalart *et al*. (1997).

This paper aims to analyze the flow characteristics around rectangular prisms. In addition, it highlights the pressure variation around the prisms with respect to different aspect ratios. There are numerous key points here. We summarize our major findings as follows. (i) For flows and wind loads around rectangular obstacles, the size and azimuth angle are very important and can be used for the design of the deployment and arrangement of a variety of buildings and structures. (ii) Despite the lack of wind-tunnel data, there are new data on mean flow, as well as data quantifying the variation of the fluctuating flow, for the single cube and rectangular obstacles. In addition, (iii) the revised paper includes much more reasonable and improved mean and turbulence quantities, as well as a quantification of the azimuthal effect of obstacles according to the DES calculation. (iv) We observed that the size and azimuth angle have a substantial effect on the surface pressure around rectangular obstacles; this phenomenon had never been previously achieved.

The contents of the paper are systematically organized as follows. First, as shown in section 2, we describe the wind tunnel experiment and the numerical simulations (i.e., the DES model calculations) around a series of rectangular prisms that were placed in an appropriate turbulent boundary layer. Second, to verify the validity of this research, we compare the wind tunnel experiment results with the numerical DES results and the existing results of previous papers, as shown in section 3.1. Third, according to both the wind tunnel experiment and the DES model results, we discuss the variation of the flow characteristics around rectangular prisms with different wind directions (in section 3.2) and aspect ratios (in section 3.3). Furthermore, section 3.4 is an analysis on the velocity and pressure spectra at the centre of the cube's top surface. Finally, section 4 presents the conclusion of this study.

## 2. Research methods and techniques

### *2.1 Five rectangular models in the tunnel*

A series of rectangular prisms are considered to be the typical representatives of the sharp-edged structures placed in a turbulent boundary layer. This study was intended to make comparisons with the existing field data from the Silsoe 6 metre cube, as shown in Richards *et al*. (2001) (hereafter, RHS). In this regard, a 1:75 scale model was used in both the wind-tunnel model and the numerical simulations. In Fig. 1, as a standard representative model, the height, width, and length of the model are all fixed to 80 mm, which is defined as 1×1 (i.e., the width over length, *w/l*, is unity). In order to compare the effects of the models with different aspect ratios, the prism width was changed but the value of the height and the length was retained, in order to observe the effect of the transverse width (see cases 2 and 3 in Table 1). In other words, because the ratio of the width to the length can be changed between 0.5, 1, and 2, it can also be defined as 1×2s, 1×1, and 2×1, respectively. As defined in cases 4 and 5, the ratio of the prism length to the height is one of

the parameters that indicate the effect of the different longitudinal lengths, such as 2×1s, 1×1, and 1×2. Note that in the Table, ‘s’ is appended to the number to denote that the length is smaller than that of the cubic model. In addition, all of these models were equipped with tubes to measure the surface pressure distribution at several salient points throughout the prism.

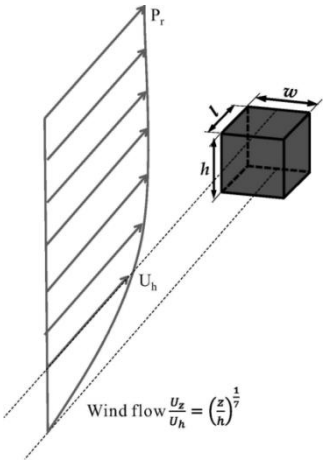


Fig. 1 Schematic diagram of the rectangular prism placed in a turbulent boundary layer. In the figure, *h*, *w*, and *l* denote the height, width, and length of the prism, respectively

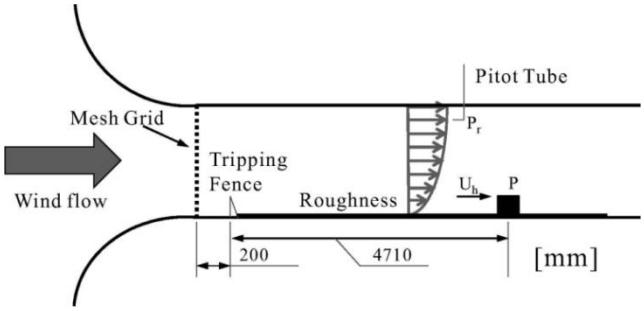


Fig. 2 Scale parameters for the scale-down models used in the study. In the table, each symbol is defined in Fig. 1

Table 1 Scale parameters for the scale-down models used in the study. In the table, each symbol is defined in Fig. 1

| Case | *w* [mm] | *l* [mm] | *h* [mm] | *w/l* | *w* × *l* [mm$^2$] | Grid nodes |
|---|---|---|---|---|---|---|
| 1 | 80 | 80 | 80 | 1 | 1 × 1 | 1,494,310 |
| 2 | 40 | 80 | 80 | 0.5 | 1 × 2s | 1,299,400 |
| 3 | 160 | 80 | 80 | 2 | 2 × 1 | 1,884,130 |
| 4 | 80 | 40 | 80 | 2 | 2 × 1s | 1,368,385 |
| 5 | 80 | 160 | 80 | 0.5 | 1 × 2 | 1,746,160 |

### *2.2 Wind tunnel measurements*

Fig. 2 illustrates the detailed set-up of the wind tunnel, and its working section is 0.6 m wide × 0.72 m high × 6 m long. The schematic diagram demonstrates the location of the grid and the tripping fence, the roughness, and the rectangular prism model. In the figure, $p$ and $p_r$ denote the static pressure on the model surface and reference pressure from the pitot tube located on the top surface at the far upstream from the model. The undisturbed wind flow $U_h$ was measured in advance by hot wire anemoetry without any model (i.e., rectangular prisms). After the wind flows around these barriers, a fully developed shear flow was obtained, which corresponded to the rural atmospheric boundary layer (more details are given by Lim 2009). This technique was often employed by wind engineering practitioners and was first devised by Cook (1978). Alternative methods to simulate atmospheric boundary layers can be seen in Hunt and Fernholz (1975). The detailed setup is described in the paper, but the major points are summarised as follows. The wind tunnel is equipped with a modern hot-wire anemometry (IFA100), a multi-channel pressure scanning system, and a Particle Image Velocimetry (PIV) system for optical measurement of the airflow. The five smooth-surface rectangular prisms used in the tunnel were made of Plexiglas and were fitted with 0.8 mm pressure taps at numerous salient points.

### *2.3 Computational techniques*

Fig. 3 depicts the schematic diagram of the numerical tunnels for cases 1×1 and 1×2 with dimensions of 7$h$ wide × 4$h$ high × 14$h$ long and 7$h$ wide × 4$h$ high ×15$h$ long, respectively. Note here that '$h$' specifically represents the characteristic length of a rectangular prism and denotes the cube height (i.e., 80 mm). The domain size, which is the entire space containing the model and the wall surface as well as the boundary conditions (e.g., velocity inlet, symmetry, periodicity, outflow, and wall conditions), is clearly shown in the figure. In terms of the fine mesh near the model wall used to resolve the small-scale turbulent flow, the first grid spacing near the wall was at 0.025$h$ and the spacing ratio was 1.1 in order to ensure the $y^+(y^+ = 35$ in the DES model) for the wall was acceptable, as suggested by Salim and Cheah (2009). In addition, when the aspect ratio of the model changes in this study, the entire domain, including the mesh grid and the model size, needs to be reconstructed, as shown in Table 1. For instance, the projection of the detailed mesh grids with a cubic model is shown in Fig. 4. Defining a suitable computational domain is a key step to correctly producing fluid dynamics phenomena such as a precise turbulent boundary layer. An overly small domain will not generate sufficient small-scale eddies around a body, while an overly large domain will unnecessarily increase the number of nodes and hence the computational time. For instance, Fig. 4 shows a projection of the detailed mesh grids with a cubic model. To reduce computational time, a parallel version was performed using FLUENT. The grid was auto-partitioned into eight parts with equal computational weights. These eight cores solved the Navier–Stokes equations for their own part of the grid. In this study, the mesh was made with ANSYS ICEM CFD 14.0, and ANSYS FLUENT 14.0 was used to solve the Navier–Stokes equations. The DES turbulence model was selected to calculate these cases. The standard wall function was applied in order to define the surface wall condition for the surfaces of the rectangular models and bottom floor wall. To evaluate the diffusive fluxes and velocity derivatives and for higher-order discretisation, we adopted a cell-based least-squares gradient scheme, which employs a Taylor expansion of the quantities of interest around each grid point and is particularly suitable for obtaining a more accurate and stable flow solution (Diskin *et al*. 2010). A

second-order implicit non-iterative time-advancement scheme was chosen to obtain time-accurate computations (Pulliam 1993). In contrast, the time step of all cases in the unsteady simulations was set to 0.0001 s. The amount of time which was discarded for the initial transient was 0.15 s, and the amount of time which was sampled statistically was 2.5 s.

In this study, we applied the DES model to calculate the internal turbulent flow from the governing equation, which is based on the Spalart-Allmaras model (i.e., S-A model) in the near-wall region. In the one-equation Spalart-Allmaras model, the transport variable $\tilde{v}$ is identical to the turbulent kinematic viscosity, except in the near-wall (viscosity-affected) region. The transport equation for $\tilde{v}$ is

$$\frac{\partial}{\partial t}(\rho\tilde{v}) + \frac{\partial}{\partial x_i}(\rho\tilde{v}u_i) = G_v + \frac{1}{\sigma_{\tilde{v}}}\left[\frac{\partial}{\partial x_j}\left\{(\mu + \rho\tilde{v})\frac{\partial\tilde{v}}{\partial x_j}\right\} + c_{b2}\rho\left(\frac{\partial\tilde{v}}{\partial x_j}\right)^2\right] - Y_v \tag{1}$$

where $G_v$ is the production of turbulent viscosity, and $Y_v$ is the destruction of turbulent viscosity that occurs in the near-wall region due to wall blocking and viscous damping, shown as follows. Other components of the equation are the following: $v$ is the molecular kinematic viscosity; $\mu$ is the turbulent viscosity; and $\sigma_{\tilde{v}}$ and $c_{b2}$ are constants valued at 2/3 and 0.622, respectively.

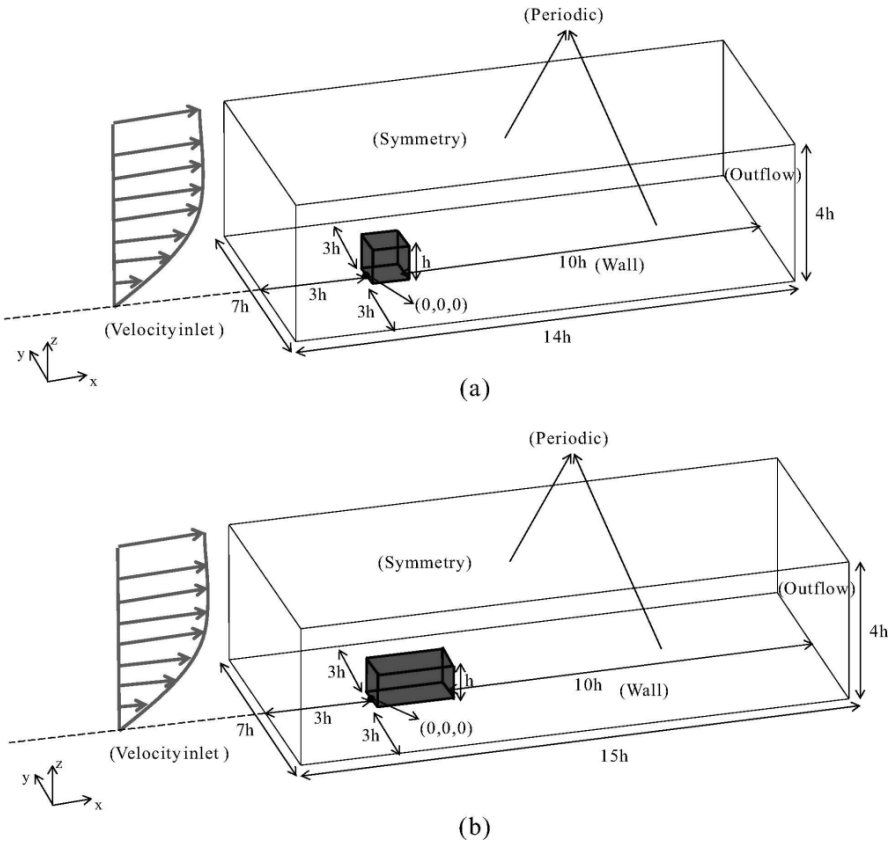


Fig. 3 Schematic diagram of the rectangular models and the domain used in the numerical tunnel: (a) case 1 ×1; (b) case 1×2

For the production of turbulent viscosity

$$G_v = c_{b1}\rho\left(S + \frac{\tilde{v}}{k^2 d^2} f_{v2}\right)\tilde{v} \tag{2}$$

where $c_{b1}$ and $k$ are constants valued at 0.1355 and 0.4187, respectively, and d is the distance from the wall. $S$ is a scalar measure of the deformation tensor and $f_{v2}$ is the viscous damping function; both are defined as follows

$$S \equiv \sqrt{2\Omega_{ij}\Omega_{ij}} + 2.0\, min\left(0, \sqrt{2S_{ij}S_{ij}} - \sqrt{2\Omega_{ij}\Omega_{ij}}\right) \tag{3}$$

$$f_{v2} = 1 - \frac{\chi}{1+\chi f_{v1}}, f_{v1} = \frac{\chi^3}{\chi^3 + {c_{v1}}^3}, \chi = \frac{\tilde{v}}{v} \tag{4}$$

where $\Omega_{ij} = \frac{1}{2}\left(\frac{\partial u_i}{\partial x_j} - \frac{\partial u_j}{\partial x_i}\right)$, $S_{ij} = \frac{1}{2}\left(\frac{\partial u_i}{\partial x_j} + \frac{\partial u_j}{\partial x_i}\right)$, and $c_{v1}$ is a constant with a value of 7.1. In addition, for the destruction of turbulent viscosity

$$Y_v = c_{w1}\rho f_w \left(\frac{\tilde{v}}{d}\right)^2 \tag{5}$$

where

$$f_w = g\left[\frac{1+{c_{w3}}^6}{g^6+{c_{w3}}^6}\right]^{\frac{1}{6}},\ g = r + c_{w2}(r^6 - r),\ r = \frac{\tilde{v}}{\tilde{s}k^2 d^2},\ \tilde{s} = S + \frac{\tilde{v}}{k^2 d^2} f_{v2} \tag{6}$$

$$c_{w1} = \frac{c_{b1}}{k^2} + \frac{(1+c_{b2})}{\sigma_{\tilde{v}}} \tag{7}$$

Here, $S$ and $f_{v2}$ are the same as defined in Eqs. (3) and (4) and $c_{w2}$ and $c_{w3}$ are constants valued at 0.3 and 2.0, respectively. These equations illuminate the fact that the length scale, $d$, plays a major role in determining the level of production and destruction of turbulent viscosity. As a 'rule of thumb', depending on the grid size, the length scale, $\tilde{d}$, replaces $d$ in the DES model, which is defined as

$$\tilde{d} = min(d,\ c_{des}\Delta) \tag{8}$$

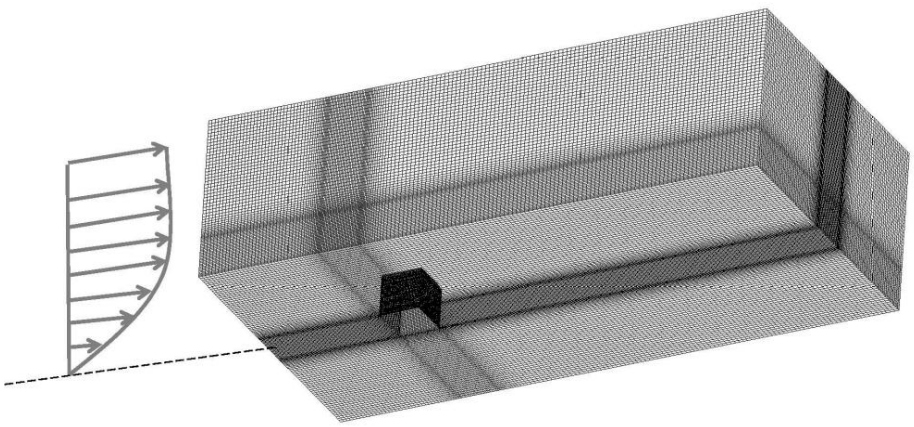

Fig. 4 Projection of the domain, including the domain/model size and outer boundary

where $d$ is dependent on the distance to the closest wall, the grid spacing, $\Delta$, is based on the largest grid space in the $x$, $y$, or $z$ directions that form the computational cell, and the empirical constant $c_{des}$ is 0.65. The DES limitations are as follows: when $c_{des}\Delta_{max} < d$ the LES model is applicable, but when $c_{des}\Delta_{max} > d$, the model switches to the RANS model (the Spalart-Allmaras model in our study).

### *2.4 Computational techniques*

In order to introduce the turbulent boundary layer at the inlet of the cube flow, it was initially generated in the channel flow without any model and at a high Reynolds number, $Re = 4.6 \times 10^4$, which is based on the cube height and the velocity at the cube height. Fig. 5 presents the streamwise velocity profiles of the mean velocity (Fig. 5(a)) and the turbulence intensity (Fig. 5(b)) obtained in the channel flow. Note that the turbulent boundary layer used to specify the inlet condition in computational techniques was obtained in the channel flow without any bodies, which was unsteadily calculated by the DES turbulence model. In addition, all information in the boundary layer was stored in the hard disk to reuse it for calculating the rectangular prism flow. The boundary layer in the domain is continuously regenerated in the channel flow, which is possible because it uses the periodic boundary condition that combines the inlet with the outlet layer and repeatedly recirculates the flow.

There are essentially two methods for generating the necessary inflow. The first is a statistical method in which a sequence of random numbers is created and then filtered to yield appropriate statistical properties and spatial correlations Xie and Castro (2008). The second involves performing a separate 'precursor' simulation of a wind environment and sampling the inflow data directly from this Lim *et al*. (2009). The second method has the desirable property that the generated inflow should naturally contain physically realistic coherent structures, so that such structures need not be produced artificially; this is the method adopted in the present work. A similar method was used by Nozawa and Tamura (2002) in their calculations of flow over a half cube. Results from the separated inflow (precursor) simulation were sampled after conditioning for approximately $50h/u_*$ and the samples were averaged spatially over the whole domain and over the period $20h/u_*$ .(see Lozano-Duran and Jimenez 2014 for a discussion of the computational domain in the streamwise direction)

For the DES results in Fig. 5(b), the values of $u'/u_h$ are obtained from modelled turbulence. The results were also compared with the existing experiments (i.e., the wind tunnel and field experiments), the calculation (i.e., the DES model), and the results from references CR and LCH. As shown in the figure, a fully developed turbulent flow was produced at the position before approaching to the rectangular prism, which was specifically designed to be similar to the (rural) atmospheric boundary layer. Fig. 5(a) shows that the wind profile is similar to the power law profile because the exponent α is approximately 0.14, which depends on the terrain roughness. The mean velocities at the cube height, $u$ and $u_{rms}$, were approximately 8 *m/s* and 0.86 *m/s*, respectively. There was a relatively high $u_{rms}$ region (i.e., almost 16%) close to the surface, but it gradually decreased with distance away from the wall. At the cube height, the turbulent intensity decreased to approximately 10.7%.

Fig. 6 presents a typical longitudinal velocity spectra, $E_u(f)$, obtained at $z = h$ for the streamwise velocity in the channel flow calculation. The results both from the wind tunnel experiments (EXP) and the DES calculations (DES) are shown in detail and compared with the common reference spectral shape, which is provided by the Engineering Sciences Data Unit

(ESDU 1985). The ESDU spectral shape is defined as

$$\frac{f \cdot E_u(f)}{u'^2} = \frac{An'}{(1+70.8n'^2)^{5/6}} \tag{9}$$

where $n' = fz/U_h$ and A is a constant with the actual value of 4. In the figure, the spectra are plotted so that the inertial sub-range of a logarithmic shape of a -5/3 fitting line spanning at least one decade collapses, which shows the energy transfer from low to high frequency. The spectrum provided by ESDU is mainly applied for a rural-type (neutrally stable) boundary layer. The cube placed in a thick turbulent boundary layer is basically located within turbulent flow. In this regard, the spectrum of turbulence should approximate the ESDU spectrum.

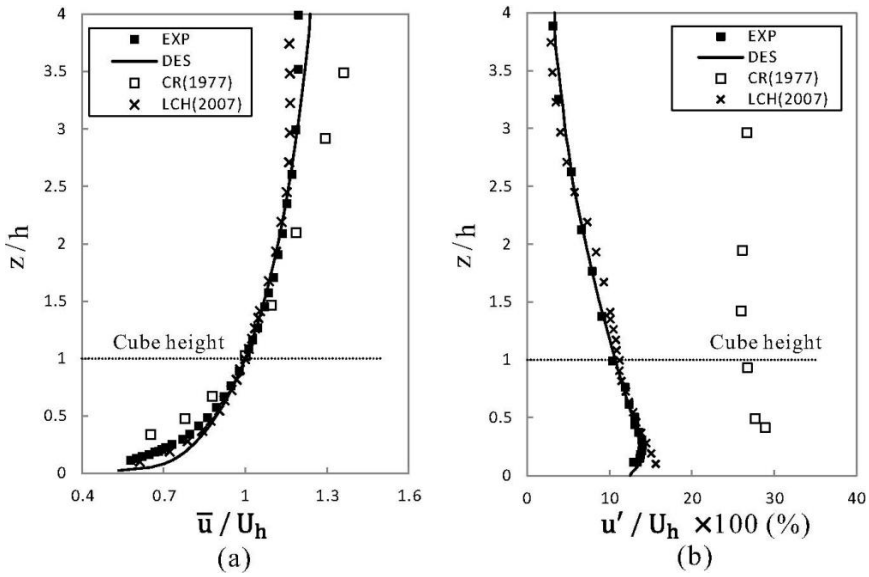


Fig. 5 Inflow boundary conditions used in the numerical tunnel: (a) the inlet mean velocity profile and (b) the turbulent intensity profile. The profiles are compared with previously existing results

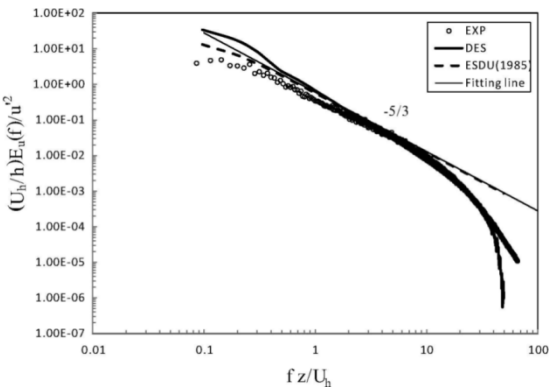


Fig. 6 Velocity spectra of the axial velocity component at z = h in the channel flow calculation. The solid lines denote the spectral curve of the ESDU and the -5/3 fitting line

## 3. Results and analysis

### *3.1 A cubic model with 0° wind direction*

In this section, we first consider a base model of a cube with an 80 mm height. For the remainder of the sections, models with different aspect ratios will be considered. In addition, a '0° wind direction' indicates that the wind direction is perpendicular to the windward side of the cube model. The dependency of the wind direction will be presented in due course. Fig. 7 shows the pressure variation around the cubic model (i.e., centre-line and transverse line) with a 0° wind direction; the coefficient of the surface pressure is defined as

$$C_p = \frac{p - p_r}{\frac{1}{2}\rho {U_h}^2} \tag{10}$$

where $p$ is the mean static pressure around the cube and $p_r$ and $U_h$ are the static pressure and streamwise velocity at the reference point, respectively. The $p_r$ and $U_h$ in reference point can be seen in Fig. 2. The reference velocity located at the cube height and the reference pressure located on the top of the tunnel. Both of them are located at further upstream of the rectangular prisms about 0.12 m. The results both along the centre-line (Fig. 7(a)) and at the mid-height (Fig. 7(b)) are strongly dependent upon the measurement location $x/h$ (from $0{\sim}1$, $1{\sim}2$, and $2{\sim}3$). Based on the analysis of the results, the mean static pressure coefficient profiles from the numerical calculation agree well (i.e., DES and $k-\varepsilon$ agree well; note that the data of the $k-\varepsilon$ model in Fig. 7 includes the results of this study's supplemental calculation). In the case of the standard $k-\varepsilon$ model, the same condition as the DES model was applied to calculate the flow domain. In addition, the standard $k-\varepsilon$ model is based on two separate transport equations for the turbulence kinetic energy ($k$) and its dissipation rate ($\varepsilon$)) have the expected shape that is consistent with the wind tunnel experiment and the existing field data of other papers (e.g., CR, LCH, and RHS). The $k-\varepsilon$ model in this study, the supplement calculation, was coaxially performed to compare the results with those of the DES model. Therefore, the results from Fig. 5 are used as the boundary conditions for the RANS simulation with the $k-\varepsilon$ model. Note that in Fig. 7(a), "WT" means 'the wind tunnel experiments in the laboratory' and "FS" means 'the field measurements from an open field site'. In addition, the numbers in bracket in the legend represent the Reynolds number. That is, 39.5 means $Re = 3.95 \times 10^5$, and 280 means $Re = 2.8 \times 10^6$. As pointed out in the paper of LCH, the higher upstream turbulence levels lead to a much earlier attachment and pressure recovery on the top surface, as well as a higher static pressure coefficient. For example, the results of CR in Fig. 7 are significantly different from the other results, which are undoubtedly a result of much higher upstream turbulence levels, as shown in Fig. 5(b). In addition, as shown in the previous studies, the largest negative pressures occur just beyond the separation region (directly to the right of the position $x/h = 1$) on the top and side surfaces and are followed by a substantial pressure recovery. The $k-\varepsilon$ model results were obtained based on the same inlet boundary conditions as the DES model; however, the $k-\varepsilon$ model results exhibit a negative peak to the right of the position $x/h = 1$. Therefore, the DES model offers a better agreement with the experimental data than the $k-\varepsilon$ model.

In order to confirm the accuracy and reliability of the results, they are compared with some existing results in other papers. Therefore, this section is a precursor for the following sections, which describe the flow around rectangular obstacles placed in different wind directions, but with identical boundary layers. In addition, Figs. 8 and 9 present the velocity distribution near the cube,

(note here that both figures are taken from DES calculations). Fig. 8 especially demonstrates the side view along the centre-line of the cube ($y = 0$), whereas Fig. 9 represents the plan view at the mid-height, $z = 0.5h$. The vertical velocity profiles in different locations generated from the wind flowing over the cube are also shown in Fig. 8(a). These profiles indicate that the flow typically separates at the leading edge and reattaches along the top surface of the cube. On the lee-side of the cube, there reversed flow exists further downstream up to approximately $x = 0.2m$; after this, the velocity profile gradually recovers to the initial inflow boundary layer. The whole streamlines along the centreline of the cube are also shown in Fig. 8(b). Because of the limitations of having a coarse resolution, the results of Lim *et al*. (2009) do not clearly show the front 'necklace' vortex.

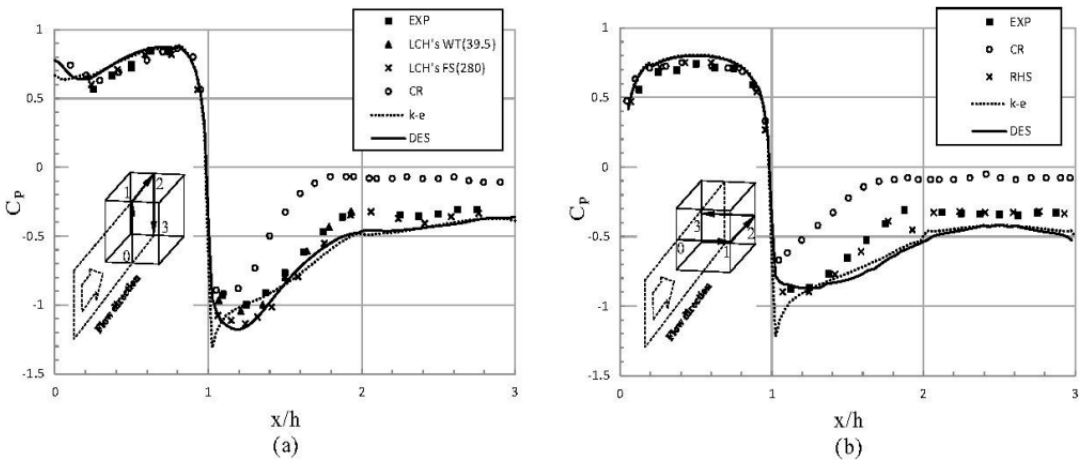


Fig. 7 Mean surface static pressure coefficient: (a) along the centreline and (b) at the mid-height

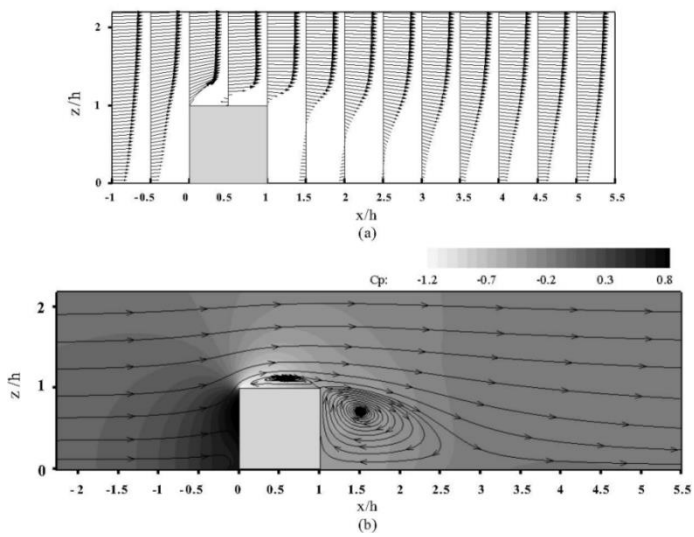


Fig. 8 Spatial distribution of the mean velocity and pressure at the central plane of the cube (y = 0): (a) mean axial velocity distribution and (b) mean static pressure contour with streamlines

However, the front necklace vortex can be observed through a different means, which will be shown in Figs. 12, 14 and 16. Note that the 'necklace' vortex appears in the windward foot of the cube. The vortex in the recirculation region on the top surface and the leeside of the cube can be observed clearly; more details can be found in Yakhot *et al*. (2006b). In Figs. 8 and 9, the darker grey colour indicates a higher pressure coefficient (see contour legend on the top right of Fig. 8(b)). The pressure contour in Fig. 8(b) also exhibits the highest pressure peak around the front top of the cube, while the lowest pressure is near the leading edge of the top surface. Obviously, the lowest peak of the pressure contour is consistent t with that of Fig. 7(a).

For the case of the plan view of the cube, Fig. 9(a) shows the velocity distribution around the cube at the mid-height of the cube plane. As the wind flow approaches the cube, the axial velocity along the transverse line is approximately uniform. At the leading sharp edge, the flow separates and forms separation regions, but no reattachment regions, along the both sides of the cube. This may be due to the lower turbulence intensity at the mid-height of the prism that is placed in a deep turbulent boundary layer. Both the lower exponent $\alpha$ and lower turbulence intensity results in a reattachment length that is larger than the range of the cube size; therefore, there is separation but no reattachment. This fact is well described in LCH and also agrees well with Gao and Chow (2005). Far downstream from the cube, the velocity profile gradually recovers to a uniform shape again. In addition, a pair of counter-rotating vortices appear on the leeside of the cube, as shown in Fig. 9(b). Because of the flow separation, the velocity near the cube wall drops significantly as compared to that in the region far away from the cube. On the leeside region of the cube, the substantial reduction in velocity leads to the formation of a pair of counter-rotating vortices. As shown in Fig. 9(b), the region with a lower velocity is called the vortex formation region, which can be seen around the cube, i.e. on the side and on the leeside of the cube. The counter-rotating recirculation vortices behind the cube and the pairs of saddle points of the recirculation vortices merge into a single saddle point along the symmetric plane.

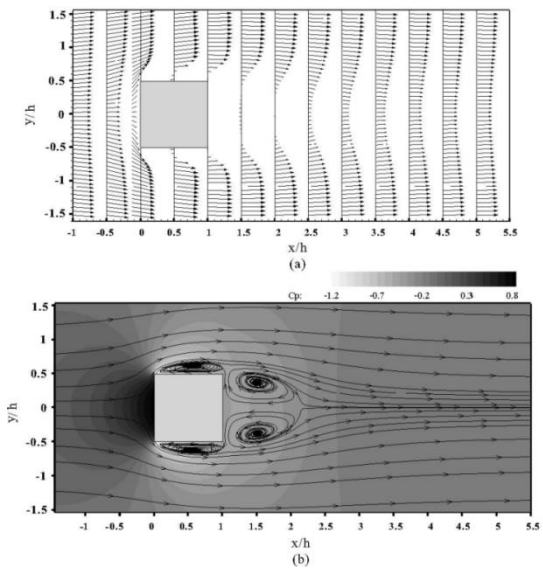


Fig. 9 Spatial distribution of the mean velocity and pressure at the horizontal plane of the cube ($z = 0.5h$): (a) mean axial velocity distribution and (b) mean static pressure contour with streamlines

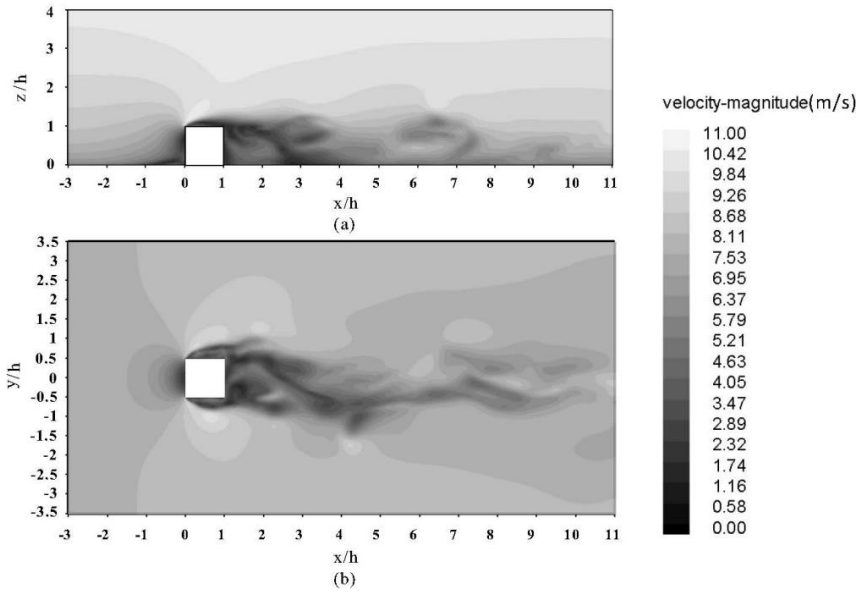


Fig. 10 Instantaneous contours of velocity at the slice of *y=0* (a) and *z=0.5h* (b) for the unsteady flow

All the results shown in Figs. 7, 8 and 9 are only time-averaged simulation data. To give an immediate impression of the "health" of the DES (i.e., to judge how well the turbulence is resolved) and also in which regions turbulence is resolved, Fig. 10 gives the visualization of an instantaneous (*t*=0.5614*s*) flow behavior of the unsteady flow. Fig. 10(a) shows the contours of velocity at $y = 0$ while Fig. 10(b) is at $z = 0.5h$. In addition, the velocity-magnitude indicated in gray color can be seen on the right side of Fig. 10. As the pictures shown, the unsteady characteristics can be seen clearly, especially in the leeside of the cube model.

### *3.2 A cubic model with different wind direction*

To investigate the effects of wind direction on the flow characteristics around the cube model, five azimuth angles (symbolized as $\phi$, with values of 0°, 10°, 20°, 30°, and 45°) were set in this study. The projection view with the wind direction can be seen in the left bottom of Figs. 11(a) and 11(c).

Although the wind direction is varied, the notations used in the graph are all the same, such as $x/h$. For a precise and relatively well-resolved calculation, a DES was performed. The effects of the wind direction on the pressure variations are shown in Fig. 11. Fig. 11(a) presents the mean static pressure coefficient along the centreline, whereas Fig. 11(c) presents the pressure distribution at the mid-height. According to the vertical black line in the position of $x/h = 0.5, 1.5,$ and $2.5$ Figs. 11(b) and 11(d) show the pressure variation with different wind directions. As shown in these figures, the DES results are generally in good agreement with the earlier data of Richards *et al*. (2007). In spite of the different wind directions, the overall pressure distributions shown in Figs 11(a) and 11(c) have the expected shape: positive values at $x/h = 0{\sim}1$; negative

values at $x/h = 1{\sim}3$; and an approximately constant level on the leeside at $x/h = 2{\sim}3$. The pressure distribution tends to vary on the surface as the wind direction changes, and is highly sensitive on the top and side surfaces. In particular, increasing the angle of the wind direction can change the pressure coefficient of the side surface at the mid-height from a negative to a positive value, as shown in Fig. 11(c). As the wind direction changes, the oncoming wind begins to turn towards the side face of the cube so that the sharp leading edge no longer generates a separated flow; rather, it faces the oncoming wind flow with a positive pressure. However, the pressure variation on the top face (see Fig. 11(a)) remains negative (i.e., no change to the positive value) although the wind direction changes so that the sharp leading edge still plays an effective role. Even along the centreline and at the mid-height of the cube the pressure coefficient decreases with an increasing angle of wind direction at the measurement locations $x/h = 0{\sim}1$ and $2{\sim}3$.

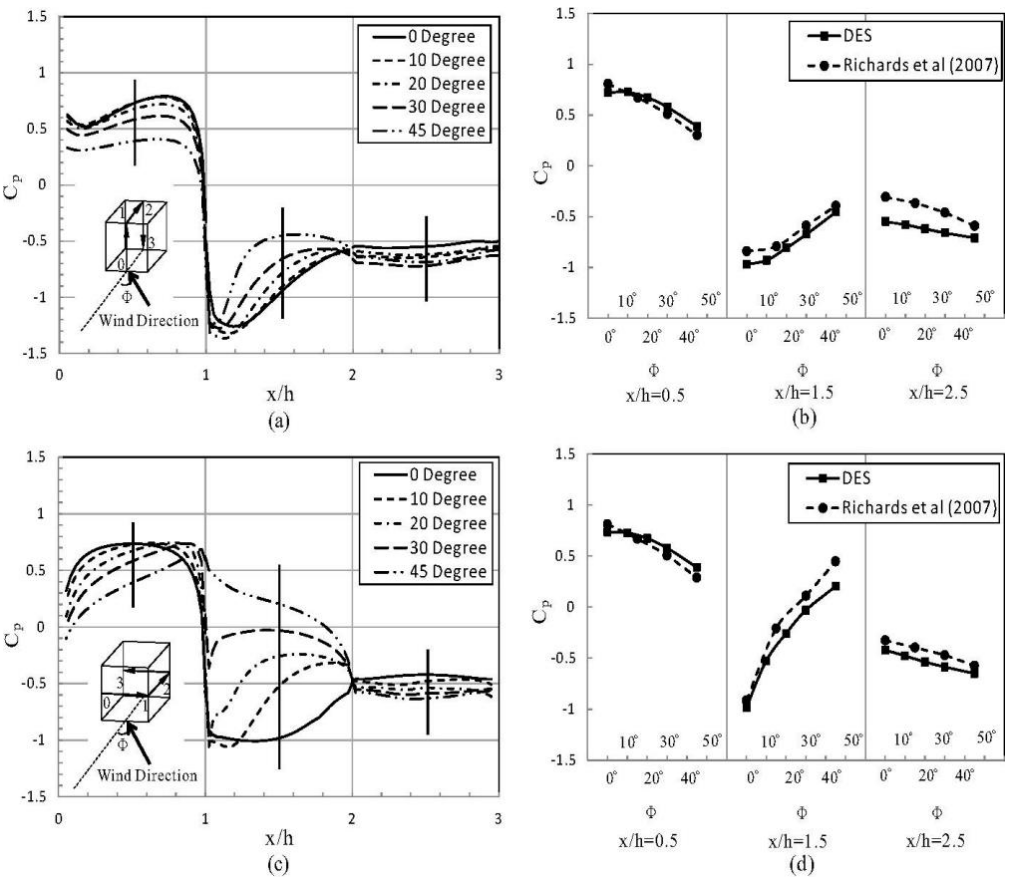


Fig. 11 Mean surface static pressure coefficient under different wind directions: (a) along the centreline and (b) at the mid-height

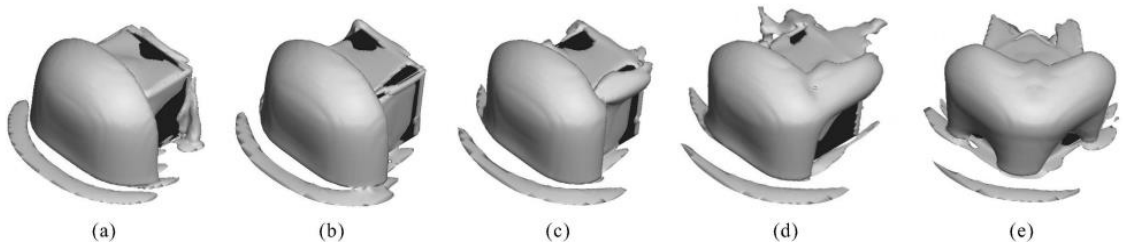


Fig. 12 Iso-surface contours of the vorticity around the cube with the varying wind directions: (a) 0°; (b) 10°; (c) 20°; (d) 30°; and (e) 45°

However, the variation in the wind direction tends to produce an opposite trend, that is, an increasing wind direction angle causes an increase in the pressure coefficient at the location $x/h = 1{\sim}2$, as indicated in Figs. 11(b) and 11(d). Regarding the difference between the results of DES and Richards *et al*. (2007) at $x/h = 1.5$, a couple of explanations can be possible to make regarding this difference. Firstly, there is an obvious difference in the upstream flow. In particular, even though the inflow mean velocity profiles are all similar, the turbulence intensities are slightly different at heights of 10%(DES) and 12% (Richards *et al*. 2007) at cube height and heights of 13% (DES) and 15% (Richards et al. 2007) at the mid-height, respectively. Note that the higher the turbulence intensity is, the lower the surface pressure is, which is almost to the same as the result in Fig. 11(d). Secondly, as noted in Lim *et al*. (2007), which includes a comparison between the cube models of 0 and 45°, strong conical vortices could be observed along the edge where two sides of the cube meet so that the surface pressure is further increased in the experiment, whereas due to the lack of precise modelling, weak conical vortices could be generated along the side corner so that the discrepancy still appears to be on the top and side surfaces.

Fig. 12 demonstrates the comparison of the three-dimensional iso-surface contours of the second invariant of the velocity gradient around the cube in different wind directions: (a) 0°; (b) 10°; (c) 20°; (d) 30°; and (e) 45°. The dark colour portrays the cube model and the grey colour signifies the *Q*-criterion (Π), which is defined as

$$\Pi = -\mathrm{L_{ij}L_{ji}} \tag{11}$$

where $L_{ij} \equiv \partial u_i / \partial x_j$. The *Q*-criterion is a measure of the regions of flow dominated by rotation rather than shear or stretching. In addition, all these figures show the instantaneous flow behaviors. These visualizations qualitatively indicate the features of the flow, which can also be seen in some existing literatures (e.g., see Lim *et al*. 2009).

In this study, the vortex indicator for different wind directions is captured with the same value (Π = 600) in the entire domain (i.e., iso-surface contour). As shown in these figures, the wind direction change causes substantial change in the resulting vortex structures around the cube. When wind flow is incident on the front face of the cube, the front iso-surface is transformed into the shape of a shield and strong large-scale rolling vortices are generated by the leading edge of the top face and side surface. As the cube gradually turns by 45°, this simple shield shape breaks into two different boulder-like piles, which are attached together. This complicated shape tells us that two conical vortices separated from the front corner of the roof and propagated far downstream. In addition, most of the calculations in Fig. 12 are made in the unsteady state so that

each figure represents a snapshot of the state of the system at a particular time, showing the general characteristics of turbulent vortices around the bodies. Due to the unsteady simulations, the plot in Fig. 12(e) may give some scatter from symmetry.

### *3.3 Models with different aspect ratios and a 0° wind direction*

In this section, we varied the aspect ratios of rectangular prisms to understand the effects of prism geometry on the flow characteristics. The aspect ratio is responsible for the shape and size of the separated wakes and, ultimately, for the structural loading and pressure, especially structure excitation. For example, the drag coefficient of an elongated rectangular prism placed in a boundary layer is a function of the elongation $l/w$ of the prism, as shown, for example, by Simiu and Scanlan (1996). In this study, we compared the numerical calculation with the tunnel data. Fig. 13 portrays the mean surface pressure distribution around the models with different transverse widths, while the other heights and lengths of the models are all equivalent. Fig. 13(a) shows the surface pressure coefficient along the centreline, while Fig. 13(b) shows the surface pressure distribution at the mid-height. The subsequent figures in Figs. 15 and 17 are arranged in the same format as Fig. 13. In the figure, the symbols denote the experimental data, the solid or dotted lines denote the DES data, and schematics showing the measurement points around the models are shown on both sides.

Fig. 13 shows how the surface pressure coefficient varies with only changing the transverse width (e.g., 0.5*h*, 1.0*h*, or 2*h*) while maintaining the area of the side face. Although the comparison of the DES model results with the experiment results has some discrepancy, the variation data tends to agree well. The immediate implication of Fig. 13 is that a wider prism geometry correlates to a stronger surface suction pressure on both the top and side surfaces. The solid arrow lines in Fig. 13 speculate the direction of the pressure drop as only the transverse width changes.

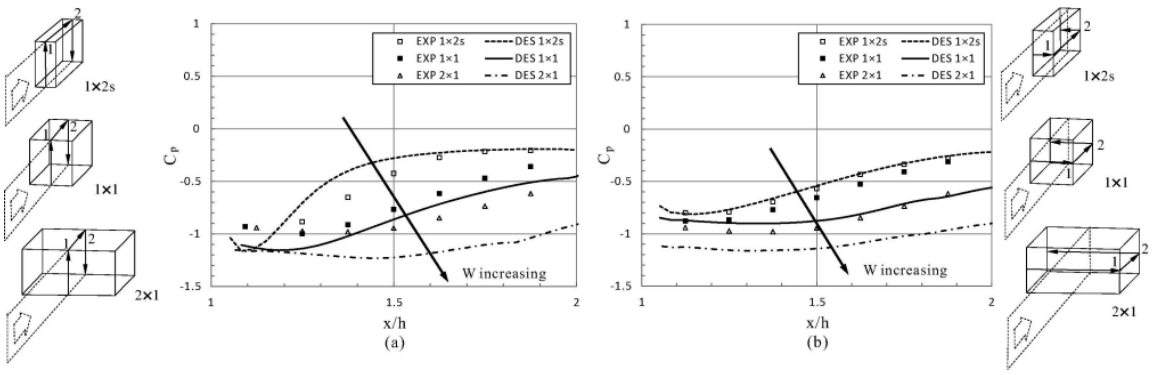


Fig. 13 Mean surface static pressure coefficient (a) along the centreline and (b) at the mid-height with only changing the transverse width

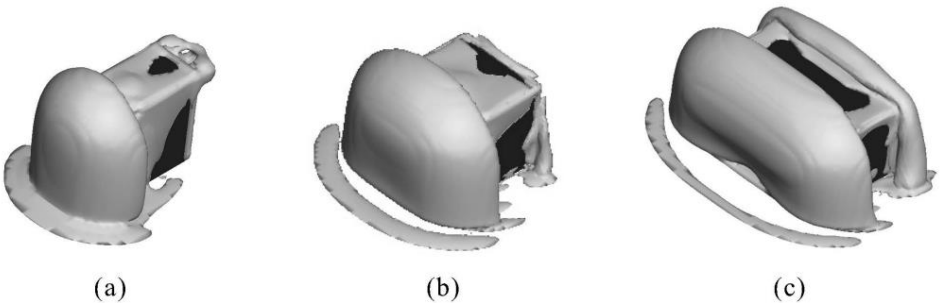


Fig. 14 Iso-surface contour plot of the vorticity around the rectangular prisms with increasing transverse width

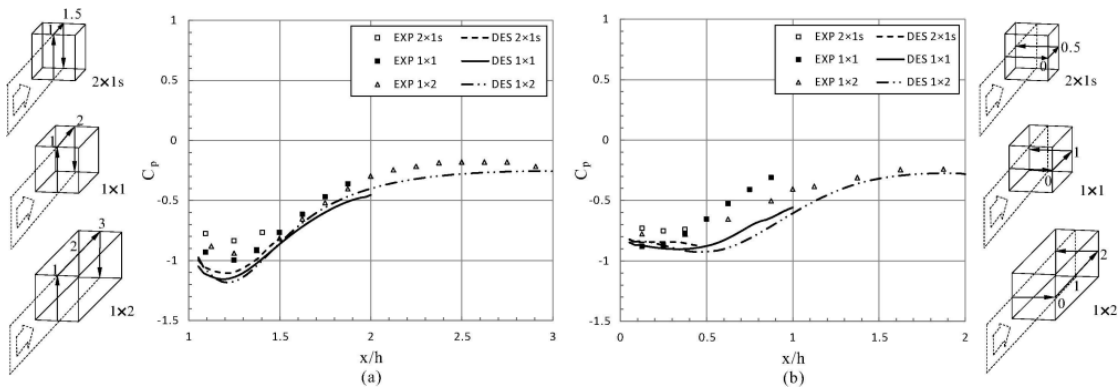


Fig. 15 Mean surface static pressure coefficient (a) along the centreline and (b) at the mid-height with only changing the longitudinal length

Furthermore, Fig. 14 illustrates the effect of only changing the transverse width on the iso-surface contours of the vorticity around the rectangular prisms. Similar to Fig. 12, the vortex indicator that is denoted by the grey colour is captured with the same value ($\Pi = 600$) at the same time. Interestingly, the 'necklace' vortex is connected to the prism when the transverse width is 0.5*h*. With increasing the transverse width, the necklace vortex becomes wider and gradually stretches to both sides in the foreside of the rectangular prism. When the transverse width is 2.0*h*, the necklace vortex strength is the weakest and begins to show signs of disappearance. With the increasing transverse width, the vortex indicator on the top surface moves to the prism edge while leaving the central region of top surface empty, as shown in Fig. 14(c).

Fig. 15 shows the variation of the surface pressure distribution around the prism after only changing the longitudinal length of the prism (e.g., 0.5*h*, 1.0*h*, or 2*h*). In this case, the value of the area of the body's frontal face is maintained. Figs. 15(a) and 15(b) show the surface pressure distribution along the centre-line and at the mid-height. As shown in the figure, the pressure distributions along the centre-line all appear similar. Although the length of the model is different, the overall distributions of the surface pressure are in good agreement. In addition, Fig. 16 also shows the iso-surface contours of the vorticity around the rectangular prisms after only changing the longitudinal length. As shown in Fig. 16, the vortex indicator ($\Pi = 600$), denoted by the grey

colour, also predicts the overall vortex structure around the prisms far downstream. The ‘necklace’ vortex in front of the rectangular prism does not vary significantly with the change in longitudinal length. When the longitudinal length is 2.0$h$, the $Q$-criterion is not sufficient to cover the entire body, as shown in Fig. 16(c).

Fig. 17 shows the results when the length and the width of the prism change, but the width over length ratio ($w/l$) is maintained. Fig. 17(a) demonstrates the pressure distribution on the top surface when $w/l$ is 0.5, and Fig. 17(b) demonstrates the distribution when $w/l$ is 2. What is emphasized here is how the scale effect of the bluff prisms depends on the wind direction (i.e., a factor of 2 in size). Therefore, while the sizes of the two models are substantially different, the ratio of the width to the length ($w/l$) remains the same. Because of this, we observed the pressure distribution on the top surface only. As shown in Fig. 17, the comparison between the experiment and the calculation reveals a much closer agreement. While there are some differences between each case, we posit that this scatter of pressure differences is caused by tunnel blockage effects. Furthermore, a larger body is far more prone to blockage effects.

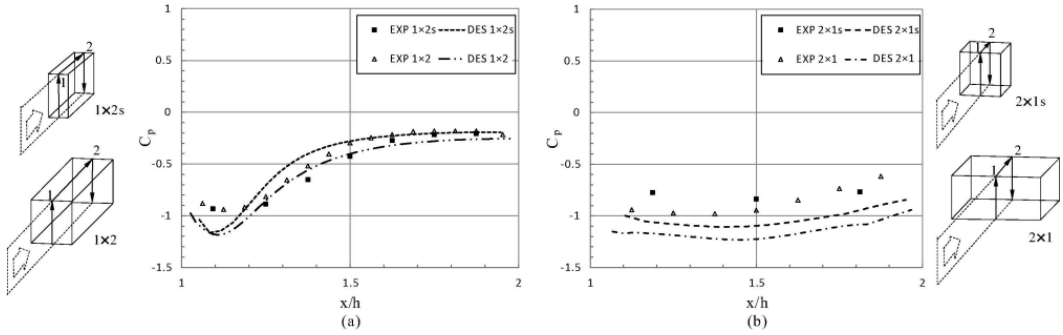


Fig. 17 Mean surface static pressure coefficient along the centreline with changing both the width and the length, but maintaining the value of *w/l*

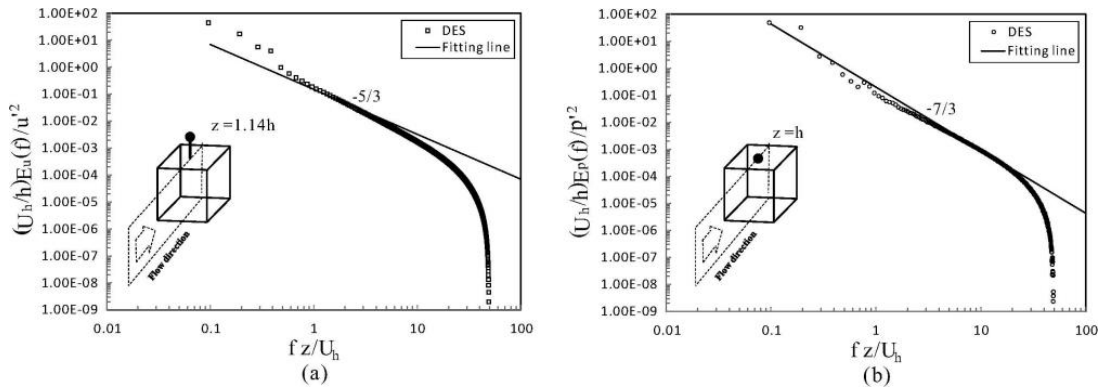


Fig. 18 Spectra distribution around the cube in 0° wind direction: (a) velocity spectra immediately above the centre of the top surface and (b) pressure spectra at the centre of the top surface

### *3.4 Spectral analysis around the cubic model*

In order to observe the flow characteristics as a function of time, the instantaneous velocity can be measured immediately above the centre of the top surface ($z = 1.14h$) and the instantaneous pressure can be measured at the centre of the top surface ($z = 1.0h$). Both measurements are taken with a small time step in the DES model (i.e., 0.0001 s). Fig. 18 shows the velocity and pressure spectra around the cubic model at a wind direction angle of 0°. In addition, as the fitting lines show in Fig. 18, the velocity spectra have an expected slope of -5/3 and the pressure spectra have an expected slope of -7/3 in the inertial sub-range region, which shows the energy transfer from low to high frequency. Furthermore, because of the numerical limitations (i.e., the limited grid resolution), both the velocity and the pressure spectra still show a rapid drop when $fz/U_h$ exceeds 25. These results are discussed in detail in the paper LCH. Although LCH contained exclusively experimental results, we observed the qualitative shape of the spectra of velocity and pressure variation over the prism so that it is worthwhile to compare the DES results with experiment.

Fig. 19 presents the spectral analysis around the cubic model in different wind directions (i.e., 0°, 10°, 20°, 30°, and 45°). In the same arrangement as Fig. 18, Figs. 19(a) and 19(b) show the velocity spectra immediately above the centre of the top surface ($\boldsymbol{z = 1.14h}$) and at the centre of the top surface ($\boldsymbol{z = h}$). Although the wind direction changes, the measurement location does not change. As mentioned in section 3.2, the flow characteristics around the cube are extremely sensitive to the wind direction. Both the velocity and the mean static pressure distribution on the top surface differ depending on the wind direction. However, as shown in Fig. 19, the spectra that are obtained from different wind directions show the expected shape and agree well with each other. That is, although the wind direction is different, the velocity and the pressure spectra are approximately same; if any, there is a negligible amount of fluctuation.

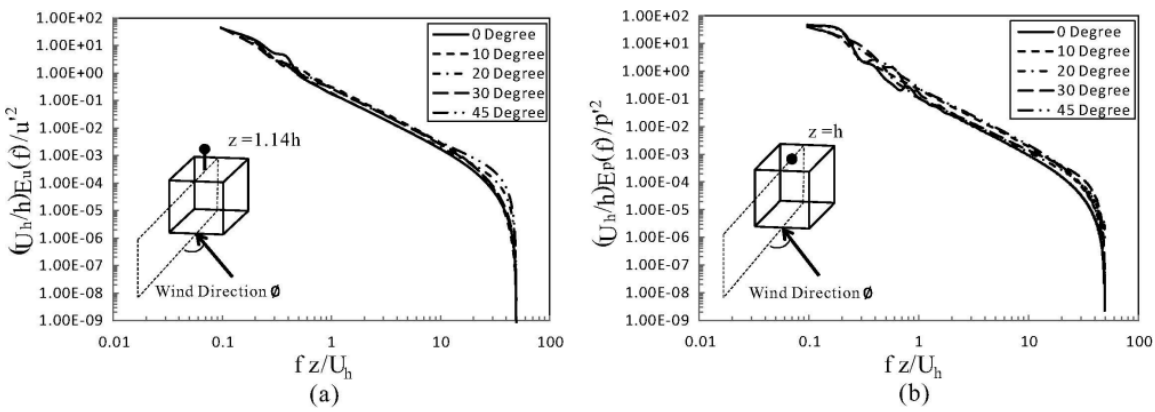


Fig. 19 Spectra distribution around the cube in different wind directions: (a) velocity spectra immediately above the centre of the top surface and (b) pressure spectra at the centre of the top surface

## 4. Conclusions

The paper presented a wind tunnel experiment and a DES calculation around rectangular prisms placed in a deep turbulent boundary layer. We summarise our major findings as follows. (i) For flows and wind loads around rectangular obstacles, the size and azimuth angle are very important and can be used for the design of the deployment and arrangement of a variety of buildings and structures. (ii) Despite the lack of wind-tunnel data, there are new data on mean flow, as well as data quantifying the variation of the fluctuating flow, for the single cube and rectangular obstacles. In addition, (iii) the revised paper includes much more reasonable and improved mean and turbulence quantities, as well as a quantification of the azimuthal effect of obstacles according to the DES calculation. (iv) We observed that the size and azimuth angle have a substantial effect on the surface pressure around rectangular obstacles. The conclusions of this study can be summarized as follows:

1. The DES results of the surface static pressure distribution are in overall agreement with the experimental results, including existing results of previous papers.
2. The turbulent flow around the rectangular prisms separates at the front edge of the prism, and then reattaches on the top and side surfaces. Multiple horseshoe and recirculation vortices are formed around the bluff prisms. Regarding the pressure distribution, the largest negative pressure occurs just beyond the separation region on the top and side surfaces, while the largest positive pressure occurs on the front surface.
3. Once the wind direction towards the bluff prisms changes, the flow characteristics are highly sensitive to the wind direction. The variations of the surface pressure and vortex structure on the top and side faces show a substantial difference.
4. The necklace vortex forms perpendicularly in the foot of the bluff prisms, and as the wind direction changes, it turns towards the wind direction but its strength and shape decrease in size. However, the velocity and pressure spectra in different wind directions show the expected shape. Alternatively, if the aspect ratio of the rectangular prism changes, the influence of the prism geometry on the flow characteristics should be considered.
5. The transverse width has a substantial effect, while the longitudinal length shows little or no influence on the surface static pressure variation. Explicitly, as the prism widens, the surface suction pressure on the top and side surfaces becomes stronger. In addition, as the transverse width increases, the necklace vortex in front of the cube widens, but its strength decreases.

Although the results presented here apply to a limited number of rectangular prisms, these conclusions may also be valid for other sharp-edged body shapes. (e.g., rectangular prisms of a wide variety of heights and aspect ratios that produce flows containing both strong and relatively steady concentrated vortices). More comparisons are still required to validate more definitive conclusions. Hence, the design of laboratory experiments intended to simulate a typical case should be undertaken.

## Acknowledgments

This work was supported by the Human Resources Development program (No. 20124010203230) of the Korea Institute of Energy Technology Evaluation and Planning (KETEP)

grant funded by the Korea government Ministry of Knowledge Economy (No. 20114010203080). In addition, this research was supported by Basic Science Research Program through the National Research Foundation of Korea(NRF) funded by the Ministry of Education, Science and Technology(2013005347). This research was also financially supported by the Ministry of Trade, Industry & Energy(MOTIE), Korea Institute for Advancement of Technology(KIAT) and DongNam Institute For Regional Program Evaluation(IRPE) through the Leading Industry Development for Economic Region.

## References

ANSYS Ltd. FLUENT User's Guide (2013), **14**, 1-2428.

Castro I.P. and Robins A.G. (1977), "The flow around a surface mounted cube in uniform and turbulent streams", *J. Fluid Mech.*, **79**, 307-335.

Cigada, A. and Malavasi, S. and Vanali, M. (2006), "Effects of an asymmetrical confined flow on a rectangular cylinder", *J. Fluid. Struct.*, **22**(2), 213-227.

Cook, N.J. (1978), "Wind tunnel simulation of the adiabatic atmospheric boundary layer by roughness, barrier and mixing device methods", *J. Wind Eng. Ind. Aerod.*, **3**(2-3), 157-176.

Diskin, B., Thomas, J.L., Nielsen, E.J., Nishikawa, H. and White, J.A. (2010), "Comparison of node-centered and cell-centered unstructured finite-volume discretizations: viscous fluxes", *AIAA J.*, **48**(7), 1326-1338.

ESDU (1985), "Characteristics of atmospheric turbulence near the ground. Part II: single point data for strong winds (neutral atmosphere)", In Engineering Sciences Data Unit.

Hunt, J.C.R. and Fernholz, H.H. (1975), "Wind-tunnel simulation of the atmospheric boundary layer", *J. Fluid Mech.*, **70**, 543-559.

Hussein, H. and Martinuzzi, R.J. (1996), "Energy balance for turbulent flow around a surface-mounted cube placed in a channel", *Phys. Fluid*, **8**(3), 764-780.

Jochen, F. and Dominic, V.T. (2008), "Hybrid LES/RANS methods for the simulation of turbulent flows", *J Prog. Aerosp. Sci.*, **44**(5), 349-377.

Larose, G.L. and D'Auteuil, A. (2008), "Experiments on 2D rectangular prisms at high Reynolds numbers in a pressurised wind tunnel", *J. Wind Eng. Ind. Aerod.*, **96**(6-7), 923-933.

Lim, H.C., Castro, I.P. and Hoxey, R.P. (2007), "Bluff bodies in deep turbulent boundary layers: Reynolds-number issues", *J. Fluid Mech.*, **571**, 97-118.

Lim, H.C. (2009), "Wind flow around rectangular obstacles with aspect ratio", *Wind Struct.*, **12**, 299-312.

Lim, H.C., Thomas, T.G. and Castro, I.P. (2009), "Flow around a cube in a turbulent boundary layer: LES and experiment", *J. Wind Eng. Ind. Aerod.*, **97**(2), 96-109.

Lozano-Duran, A. and Jimenez, J. (2014), "Effect of the computational domain on direct simulations of turbulent channels up to $Re_\tau$ =4200", *Phys. of fluids*, **26**(1), 011702.

Martinuzzi, R. and Tropea, C. (1993), "The flow around surface-mounted, prismatic obstacles placed in a fully developed channel flow", *J. Fluid Eng – T ASME.*, **115**(1), 85-92.

Matsumoto, M. and Yagi, T. and Tamaki, H. and Tsubota, T. (2008), "Vortex-induced vibration and its effect on torsional flutter instability in the case of B/D = 4 rectangular cylinder", *J. Wind Eng. Ind. Aerod.*, **96**(6-7), 971-983.

Nozawa, K. and Tamura, T. (2002), "Large eddy simulation of the flow around a low-rise building immersed in a rough-wall turbulent boundary layer", *J. Wind Eng. Ind. Aerod.*, **90**(10), 1151-1162.

Pulliam, T. (1993), *Time Accuracy and the Use of Implicit Methods*, AIAA Paper 93-3360-CP.

Richards, P.J. and Hoxey, P.J. and Short, L.J. (2001), "Wind pressure on a 6m cube", *J. Wind Eng. Ind. Aerod.*, **89**(14-15), 1553-1564.

Richards, P.J., Hoxey, R.P., Connell, B.D. and Lander, D.P. (2007), "Wind-tunnel modelling of the Silsoe cube", *J. Wind Eng. Ind. Aerod.*, **95**(9-11), 1384-1399.

Rodi, W. (1997), "Comparison of LES and RANS calculations of the flow around bluff bodies", *J. Wind Eng. Ind. Aerod.*, **69**, 55-75.

Salim, S.M. and Cheah, S.C. (2009), "Wall $y^+$ strategy for dealing with wall-bounded turbulent flows", *Proceedings of the International MultiConference of Engineers and Computer Scientists, IMECS 2009*, Hong Kong.

Simiu, E. and Scanlan, R.H. (1996), *Wind effects on structures – Fundamentals and applications to design*, 3rd Ed., John Wiley, New York, USA.

Schofield, W. and Logan, E. (1990) "Turbulent shear flow over surface-mounted obstacles", *J. Fluid Eng.- T ASME*, **112**(4), 376-385.

Spalart, P.R., Jou, W.H., Strelets, M. and Allmaras, S.R. (1997), "Comments on the feasibility of LES for wings, and on a hybrid RANS/LES approach, Advances in DNS/LES", *Proceedings of the 1st AFOSR Int. Conf On DNS/LES*, Greyden Press, Columbus, OH, United States.

Tieleman, H.W. and Akins, R.E. (1996), "The effect of incident turbulence on the surface pressures of surface-mounted prisms", *J. Fluid. Struct.*, **10**(4), 367-393.

Tominaga, Y. and Stathopoulos, T. (2010), "Numerical simulation of dispersion around an isolated cubic building: Model evaluation of RANS and LES", *Build. Environ.*, **45**(10), 2231-2239.

Xie, Z.T. and Castro, I.P. (2008), "Efficient generation of inflow conditions for large-eddy simulations of street-scale flows", *Flow Turbul. Combust.*, **81**(3), 449-470.

Yakhot, A., Anor, T., Liu, H. and Nikitin, N. (2006a), "Direct numerical simulation of turbulent flow around a wall-mounted cube: spatio-temporal evolution of large-scale vortices", *J. Fluid Mech.*, **566**, 1-9.

Yakhot, A., Liu, H. and Nikitin, N. (2006b), "Turbulent flow around a wall-mounted cube: A direct numerical simulation", *Int. J. Heat Fluid Fl.*, **27**(6), 994-1009.

*JH*